2021-06

COMPENSATION THROUGH PREDICTION FOR ATMOSPHERIC TURBULENCE EFFECTS ON TARGET IMAGING AND HIGH ENERGY LASER BEAM

Zhang, Jun H.

Monterey, CA; Naval Postgraduate School

NAVAL POSTGRADUATE SCHOOL

MONTEREY, CALIFORNIA

THESIS

COMPENSATION THROUGH PREDICTION FOR ATMOSPHERIC TURBULENCE EFFECTS ON TARGET IMAGING AND HIGH ENERGY LASER BEAM

by

Jun H. Zhang

June 2021

Thesis Advisor: Jae Jun Kim
Co-Advisor: Brij N. Agrawal

THIS PAGE INTENTIONALLY LEFT BLANK

REPORT DOCUMENTATION PAGE			*Form Approved OMB No. 0704-0188*

1. AGENCY USE ONLY *(Leave blank)*	**2. REPORT DATE** June 2021	**3. REPORT TYPE AND DATES COVERED** Master's thesis

4. TITLE AND SUBTITLE COMPENSATION THROUGH PREDICTION FOR ATMOSPHERIC TURBULENCE EFFECTS ON TARGET IMAGING AND HIGH ENERGY LASER BEAM	**5. FUNDING NUMBERS**
6. AUTHOR(S) Jun H. Zhang	
7. PERFORMING ORGANIZATION NAME(S) AND ADDRESS(ES) Naval Postgraduate School Monterey, CA 93943-5000	**8. PERFORMING ORGANIZATION REPORT NUMBER**
9. SPONSORING / MONITORING AGENCY NAME(S) AND ADDRESS(ES) N/A	**10. SPONSORING / MONITORING AGENCY REPORT NUMBER**

11. SUPPLEMENTARY NOTES The views expressed in this thesis are those of the author and do not reflect the official policy or position of the Department of Defense or the U.S. Government.

12a. DISTRIBUTION / AVAILABILITY STATEMENT Approved for public release. Distribution is unlimited.	**12b. DISTRIBUTION CODE** A

13. ABSTRACT (maximum 200 words)

Atmospheric turbulence significantly degrades the performance of High Energy Laser (HEL) beams. The three key undesirable effects are: (1) degraded target images used for target tracking; (2) inaccurate HEL pointing; and (3) reduction in HEL power during propagation to the target. The current approach for compensating for these turbulence effects uses adaptive optics to measure atmospheric turbulence and compensate the aberration in the optical beam. However, an adaptive optics system has limited performance in strong turbulence and an optical system makes the HEL system more complex. With improvements in Deep Learning algorithms and further development in Artificial Intelligence, we used Deep Learning and Convolutional Neural Networks to predict the atmospheric turbulence and compensate for its negative effects on laser beams. The predicted turbulence can be used for image correction and HEL beam correction using a deformable mirror to reduce turbulence effects during propagation.

14. SUBJECT TERMS High Energy Laser Beam, HEL, atmospheric turbulence, adaptive optics, artificial intelligence, deep learning	**15. NUMBER OF PAGES** 63
	16. PRICE CODE

17. SECURITY CLASSIFICATION OF REPORT	**18. SECURITY CLASSIFICATION OF THIS PAGE**	**19. SECURITY CLASSIFICATION OF ABSTRACT**	**20. LIMITATION OF ABSTRACT**
Unclassified	Unclassified	Unclassified	UU

NSN 7540-01-280-5500

Standard Form 298 (Rev. 2-89)
Prescribed by ANSI Std. 239-18

THIS PAGE INTENTIONALLY LEFT BLANK

Approved for public release. Distribution is unlimited.

COMPENSATION THROUGH PREDICTION FOR ATMOSPHERIC TURBULENCE EFFECTS ON TARGET IMAGING AND HIGH ENERGY LASER BEAM

Jun H. Zhang
Major, Republic of Singapore Navy
BSME, National University of Singapore, 2011

Submitted in partial fulfillment of the
requirements for the degree of

MASTER OF SCIENCE IN MECHANICAL ENGINEERING

from the

NAVAL POSTGRADUATE SCHOOL
June 2021

Approved by: Jae Jun Kim
Advisor

Brij N. Agrawal
Co-Advisor

Garth V. Hobson
Chair, Department of Mechanical and Aerospace Engineering

THIS PAGE INTENTIONALLY LEFT BLANK

ABSTRACT

Atmospheric turbulence significantly degrades the performance of High Energy Laser (HEL) beams. The three key undesirable effects are: (1) degraded target images used for target tracking; (2) inaccurate HEL pointing; and (3) reduction in HEL power during propagation to the target. The current approach for compensating for these turbulence effects uses adaptive optics to measure atmospheric turbulence and compensate the aberration in the optical beam. However, an adaptive optics system has limited performance in strong turbulence and an optical system makes the HEL system more complex. With improvements in Deep Learning algorithms and further development in Artificial Intelligence, we used Deep Learning and Convolutional Neural Networks to predict the atmospheric turbulence and compensate for its negative effects on laser beams. The predicted turbulence can be used for image correction and HEL beam correction using a deformable mirror to reduce turbulence effects during propagation.

THIS PAGE INTENTIONALLY LEFT BLANK

TABLE OF CONTENTS

LIST OF FIGURES

LIST OF TABLES

THIS PAGE INTENTIONALLY LEFT BLANK

LIST OF ACRONYMS AND ABBREVIATIONS

AI	Artificial Intelligence
AO	Adaptive Optics
CNN	Convolutional Neural Networks
DE	Directed Energy
DL	Deep Learning
DM	Deformable Mirror
FEL	Free Electron Laser
FPS	Frames Per Second
HEL	High Energy Laser
MNIST	Modified National Institute of Standards and Technology
PSF	Point Spread Function
ReLU	Rectified Linear Unit
ResNet	Residual Network
SSIM	Structural Similarity Index of Image
SSL	Solid State Laser
UAV	Unmanned Aerial Vehicle

THIS PAGE INTENTIONALLY LEFT BLANK

ACKNOWLEDGMENTS

I would like to thank my advisors, Dr. Jae Jun Kim and Dr. Brij Agrawal, for their kind guidance and support in this research. Without their expertise and assistance, this research would not have been possible. I would also like to thank Dr. Leonardo Herrera for helping with some coding challenges and specific implementation assistance.

I would also like to thank the Naval Postgraduate School for an excellent immersive learning environment where I have been challenged through many aspects of applying what I have learnt into solving real-world problems.

Finally, I would like to thank the Singapore Navy for giving me the opportunity to further my studies at Naval Postgraduate School and the unwavering support it rendered during the pandemic.

THIS PAGE INTENTIONALLY LEFT BLANK

I. INTRODUCTION

High Energy Laser (HEL) systems have immense potential in military applications due to its unlimited rounds, precision strike and speed of attack. HEL systems had been extensively evaluated and can potentially be effectively against traditional threats like missile strikes and adversarial ships (O'Rourke 2015). In addition, asymmetric threats like drone strikes, small boat swarm attacks and terrorist suicide bombing are also potential areas for meaningful use of HEL. The successful deployment of a HEL system is also imperative given that these asymmetric threats are rapidly evolving in the combat environment. While traditional weapons like precision missiles are effective against these threats, they are usually too costly per round. Other lower cost weapon types lack the accuracy, precision, and speed to effectively neutralize such threats. Thus, HEL systems present an opportunity for the use of high precision and low-cost per round offensive means against both traditional and evolving threats in the military environment (Ang 2012; Valiani 2016).

However, HEL systems do not come without limitations and deployment on naval warships has continued to be challenging (Fussman 2014; Corley 2010). As an optical system, the HEL is affected greatly by transmission losses in the system and the environment the laser travels through. The laser beam can be rendered ineffective at the target. Up to 60% of the original emitted power could be lost at the target even before accounting for reflected power at the target (Bahman 2016, 49). To increase its effectiveness, atmospheric turbulence effects need to be compensated in the laser beam. Current technologies for beam correction are limited by the wavefront sensor's resolution and the increasing capital cost to improve correction via the number of correction elements in the wavefront sensor. However, with the advent of Artificial Intelligence (AI) and Deep Learning (DL) for image correction (He et al. 2015), an opportunity to improve image quality and beam effectiveness is available.

This thesis investigates the use of AI tools like Convolutional Neural Networks (CNN) and DL in predicting atmospheric turbulence for laser beam correction to increase

the effectiveness of a HEL system. First, a simplified optical model is conceived and used as a testbed to evaluate prediction performance of atmospheric turbulence. In particular, a point light source on a target and the corresponding Point Spread Function (PSF) image is generated for training the network. Zernike polynomials are used to represent the wavefront error of the light caused by the atmospheric turbulence. Second, the trained network is applied to simulated real-life Unmanned Aerial Vehicle (UAV) images dataset for Mongoose and Reaper UAVs. Third, a model is proposed for direct image correction of blur image caused by atmospheric turbulence to clear pristine image to improve target tracking in the HEL system.

The computer simulations conducted in this thesis were based on MATLAB's DL toolbox and architecture. For future research work, the model can be reproduced in a laboratory environment to evaluate the model's effectiveness in predicting atmospheric turbulence before applying it in field tests and evaluations.

II. BACKGROUND

A. HEL SYSTEMS OVERVIEW

HEL systems are a very broad classification of laser systems deployable on navy ships and other military platforms. These systems can range from power ratings of about 10kW to the MW range. 10kW laser systems are effective against "soft" UAVs without any hardened skin while MW lasers can be effective against anti-ship missiles and ballistic missiles up to 10 nautical miles (O'Rourke 2015). The below section summarizes the types of laser systems being considered by the Navy.

1. Types of Laser Systems under Consideration by the Navy

There are three different types of laser weapons being considered for deployment in the Navy (O'Rourke 2015; Valiani 2016). Table 1 shows a summary of the respective laser types and its key attributes for cost and deploy-ability on a navy ship. Essentially, Fiber Solid State Laser (SSL) is a common industrial laser which could be easily deployed in a ship but is limited in range and effectiveness against targets which require higher power. Slab SSL can be scaled up to 100kW in power and have ranges further than Fiber SSL. Free Electron Laser (FEL) is scalable to the MW range which makes it effective against anti-ship missiles and ballistic missiles. However, it is costly and difficult to retrofit on existing ship platforms and likely needs to be integrated into new ship classes in future builds.

Table 1. Types of Lasers. Source: O'Rourke (2015).

Laser Type	Current Typical Power / kW	Cost Factor	Deploy-ability	Additional Remarks
Fiber SSL	Tens of kW	Low	High	Commonly used in industry for cutting and welding metals.
Slab SSL	100kW	Medium	Medium	Good Beam Quality, longer range,
FEL	MW	High	Low	Adjustable wavelength Too large to fit in ship

As a proof of concept and for evaluation of a HEL system deployed in an operational environment, the USS *Ponce* (LPD 15), was installed with a Fiber SSL laser system in Aug 2014 and much success was reported. The system was reported to be highly reliable and maintainable. Also, the cost per shot was less than a dollar and the system was proven to be effective against swarm boats or UAVs (O'Rourke 2015). Figure 1 shows a photograph of the system deployed in the USS *Ponce*.

Figure 1. Photograph of HEL Deployed in USS *Ponce*. Source: O'Rourke (2015).

2. Limitations of HEL Systems

Although HEL systems have immense potential to be deployed in the maritime environment and in a naval warship, laser systems still have limited effectiveness in countering threats due to line-of-sight engagement requirements and beam weakening effects due to presence of air molecules in the atmosphere (Bahman 2016, 50; Fussman 2014). Since laser light propagates through the atmosphere on a straight path, HEL systems cannot be used for over-the-horizon targeting or targets that are blocked by objects in the middle. Consequently, small boats that gets blocked by undulating waves or targets block by other ships in between cannot be engaged by the system. Additional own ship maneuvers will be required for target engagement.

Atmospheric effects are another limitation of the HEL system. The presence of air molecules, water vapor and salt particles in the maritime environment significantly alters the beam focus and reduces the effective range of a laser. In addition, atmospheric turbulence can also be caused by variations in the index of refraction in the atmosphere, causing further degradation of the laser beam during its propagation through the atmosphere. While the FEL wavelength can be adjusted to reduce the atmospheric absorption by water vapor, it is not yet a practical solution for existing naval platforms. Fiber and Slab SSL lasers cannot adjust its wavelengths and could not be utilized to maximize the range of the laser. (Ang 2012).

Adaptive Optics (AO) systems with wavefront sensors and Deformable Mirrors (DM) are required to correct the atmospheric turbulence before the beam propagates through the atmosphere to reduce the effects of turbulence. This correction makes the HEL system more complex and harder to deploy on warships, which has limited physical space for a complex system. See Section C for a review of AO systems used in laser beam correction.

B. ATMOSPHERIC EFFECTS ON HEL

Due to the presence of air molecules and the inhomogeneity in temperature, density and other properties, laser intensity at the target can be reduced significantly (Puent 2017; Fussman 2014). These effects are briefly explained below. See (Bahman 2016, 379–387)

for a comprehensive review. The scope of this research focuses on correcting the laser against atmospheric turbulence effects.

1. Atmospheric Turbulence

Atmospheric turbulence is primarily caused by fluctuations in the index of refraction of air in the atmosphere. Strong atmospheric turbulence is present in the maritime environment and can result in significant power loss. For the laser beam to propagate through the maritime environment and maintain its power, atmospheric turbulence effects need to be measured and the laser beam corrected for the laser to be an effective countermeasure (Liu, Lopez, and Spalding 2020; Xu et al. 2019). The means of modelling atmospheric turbulence is discussed in Chapter IV.

2. Thermal Blooming

Another prominent effect when laser propagate through the atmosphere is thermal blooming. It is a heat-induced change in the optical parameters of the medium that lead to changes in radiation propagation (Bahman 2016, 380). Thermal blooming effects are nonlinear and are generally harder to reproduce in a simulated computer environment. Hence, this study does not include the effects of thermal blooming. Further findings and discussions on the thermal blooming in aerosols are found in (Palmer 1980).

C. ADAPTIVE OPTICS

The concepts of optics and adaptive optics are required to better explain the study. Figure 2 shows a graphical representation of two cases with and without atmospheric turbulence in the atmosphere. The wavefront is represented as an imaginary surface representing points of a wave that vibrate in unison. When wavefronts of a point source pass through an ideal atmosphere with no turbulence, the resulting image observed at the telescope is a focused airy disk. However, with turbulence, the resulting telescope image is an aberrated image with distortion. The telescope images of these point sources are also referred to as PSF images.

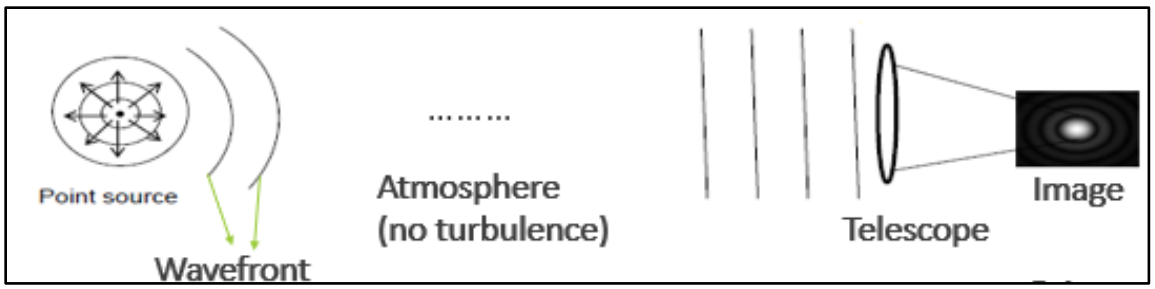

(a)

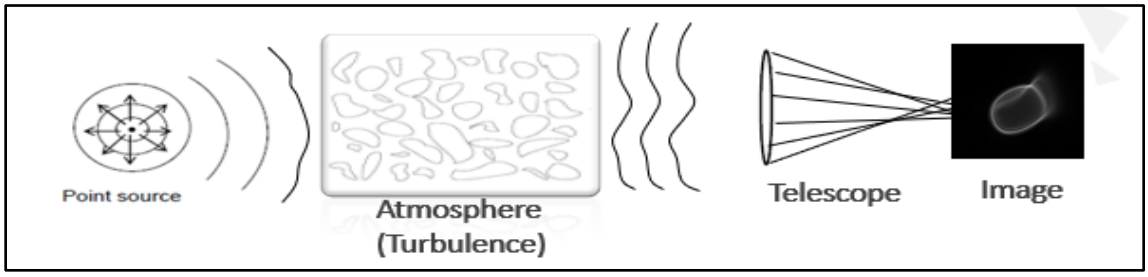

(b)

Figure 2. Graphical Representation of Atmospheric Turbulence and Telescope Image: No Turbulence (a), and Presence of Turbulence (b)

Figure 3 shows a conventional AO component in a laser system. To mitigate atmospheric turbulence effects, AO is used to correct laser beams before the beam propagates through the atmosphere. The conventional AO system uses a wavefront sensor to detect the atmospheric turbulence by measuring light captured at the system and formulating the wavefront that it received. For a Shack-Harmann wavefront sensor shown in Figure 3, an array of lens capture light from the target and interpolates the received wavefront. Coupled with a processing computer, the wavefront is re-constructed, the conjugate of the re-constructed wavefront is then fed to the DM to correct the laser beam before propagating it through the atmosphere to the target (Murray 2006).

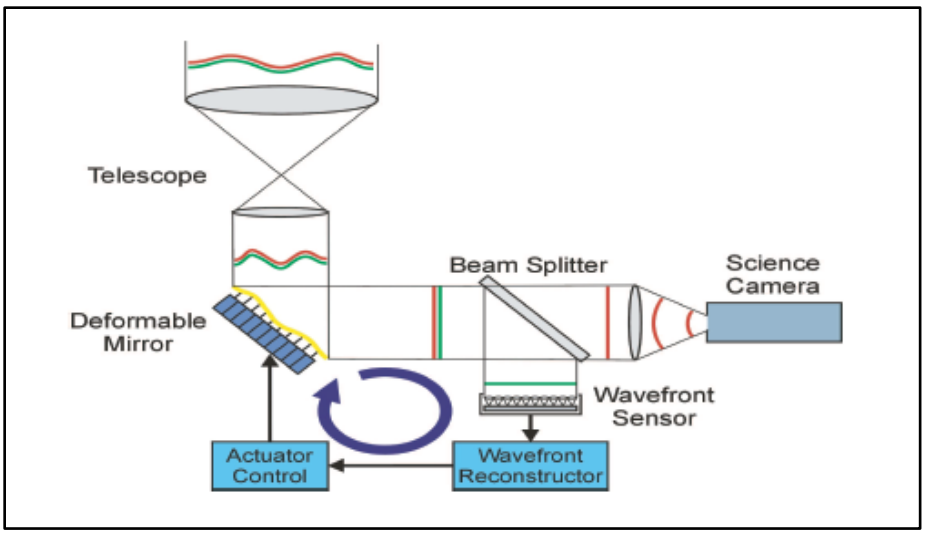

Figure 3. A Conventional AO System. Source: Murray (2006).

While somewhat effective in correcting the laser beam, the AO system is complex and requires additional hardware like the wavefront sensor for detection of wavefronts. The wavefront sensor is also limited by hardware in terms of resolution given the fixed amount of lens available in the sensor for detecting light beams. Given these limitations, the use of DL and state-of-the-art CNN could perform better in constructing the wavefront and correcting the laser beam. Wavefront sensing and correction is covered in greater detail in Chapter IV.

D. ARTIFICIAL INTELLIGENCE AND DEEP LEARNING

An alternative to direct wavefront sensing is the use of state-of-the-art correction algorithms to apply aberration adjustments directly to the target image. With the advent of CNN and DL (Nishizaki et al. 2019; He et al. 2015), it is possible to predict atmospheric aberrations using trained CNN on a large dataset of pre-defined images.

CNN are a rapidly developing field of machine learning where deep neural networks are used to predict outcomes given a set of training data. Most CNN applications are in object classifications and output regression. CNN used for classification can be adapted to perform regressive tasks by fitting the input images to the correct sizes and changing the output layer to perform regression instead of classification.

Deep learning is the process of training the machine to identify key image features and using these features to make regressive output decision. In order to ensure good output results from deep learning, the training dataset must be sufficiently large and general so that the model is not overfitted on the training data.

Chapter III will describe in greater detail the use of AI and DL in HEL systems applications.

E. RESEARCH OBJECTIVES

The two objectives of this research are to develop a computer integrated wavefront sensor that precisely predicts the wavefront aberrations due to atmospheric effects and introduce active correction to the laser before its propagation through the atmosphere to the target. This would greatly improve the laser intensity at the target and hence increase the lethality of the HEL system if deployed on a warship. In addition, with improved wavefront sensing, the HEL system can be simplified without the wavefront sensor but yet provide high resolution wavefront correction.

THIS PAGE INTENTIONALLY LEFT BLANK

III. APPLICATIONS OF AI IN HEL SYSTEMS

This chapter describes in greater detail how Artificial Intelligence (AI) can be applied in HEL systems to improve accuracy of the laser and help increase the effectiveness of the laser beam. The potential improvements using AI are twofold. First, atmospheric turbulence could be predicted using techniques available in image processing. Using blurred images that were "captured" from exposure to atmospheric turbulence, the DL model could back propagate these results and predict the atmospheric turbulence that the image was subjected to. Second, the target image blurred by atmospheric turbulence can be directly corrected using DL to improve the target's image on the output of the tracking system and can help improve target tracking, which eventually leads to better effectiveness of the laser beam.

A. DEEP LEARNING AND CNN

AI generally refers to any form of technology that incorporates some form of intelligent learning process that allows machines and computers to mimic the construct and learning capabilities of the human mind (IBM Cloud Education 2021). AI is a very broad field of study and would include many evolving and state-of-the-art techniques newly developed. DL is an aspect of AI that uses deep neural networks to figure out a model based on data.

For the human mind, it is reasonably easy to recognize images of handwritten numbers shown in Figure 4. However, this task would be extremely challenging for computers since these handwritten numbers vary subtly in terms of orientation, size, and style. Computers "view" images as a 2-dimensional (black and white images) or 3-dimensional (colored images) array of numbers. The array size depends on the resolution of the image while the numbers in each pixel represents the color tone.

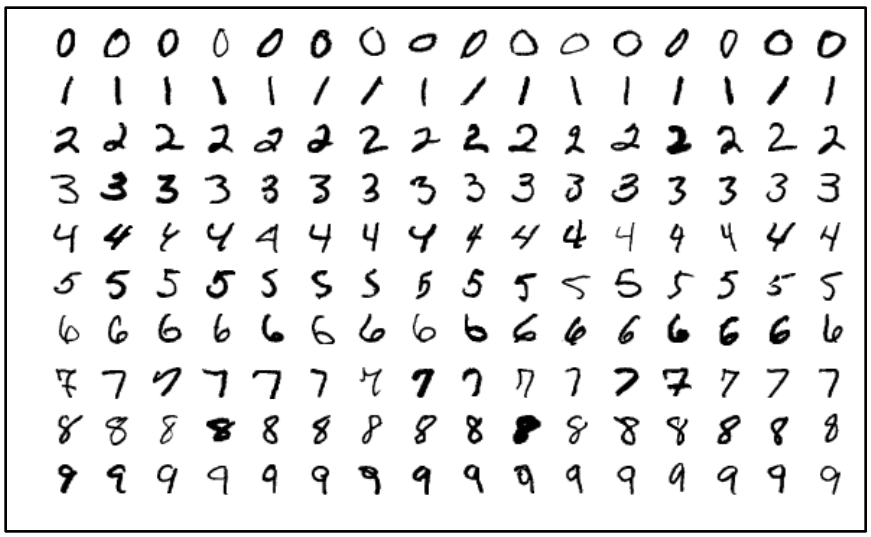

Figure 4. Some Handwritten Numbers. Source: MNIST Database (n.d.).

Hence, for computers to recognize images, a different approach is required. The concept of neural networks is conceived and first proposed in 1944 (Brij Agrawal, personal communication, October 27, 2020). The neural network models the neurons in a biological brain and multiplies incoming data and sum it. A nonlinear activation function is applied to the output of the neuron, if the output is above a certain preset value, the information is passed to the next connection, otherwise, no information is passed. Figure 5 illustrates this single node in a neural network. This node is the main building block for neural networks. A number of different activation functions can be used but typically, the Rectified Linear Unit (ReLU) activation function, shown in the figure, is chosen as it does not saturate and converges much faster than other functions.

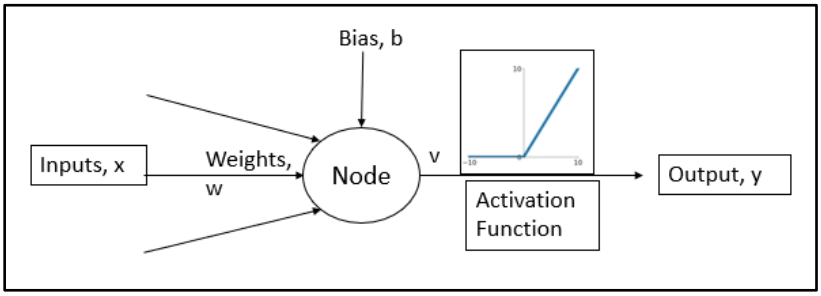

Figure 5. Design of a Node in Neural Networks

The mathematical operation of a node can be represented as

$$\begin{aligned} v &= \mathbf{w}\mathbf{x} + b \\ y &= \varphi(v) \end{aligned}, \tag{1}$$

where $\varphi(v)$ is the activation function and vectors **w** and **x** are defined as

$$\begin{aligned} \mathbf{w} &= \begin{bmatrix} w_1 & w_2 & w_3 \end{bmatrix} \\ \mathbf{x} &= \begin{bmatrix} x_1 \\ x_2 \\ x_3 \end{bmatrix} \end{aligned}. \tag{2}$$

The ReLU activation function is represented as follows.

$$\varphi(v) = \begin{cases} x, x > 0 \\ 0, x \le 0 \end{cases}. \tag{3}$$

Also, the bias, *b,* represents the bias of certain nodal inputs and can be used to place more weightage on some nodes that are known to contribute to be more important in determining relationships between layers. It also affords flexibility to the model to learn more complex input-output relations.

A neural network is made up of thousands to millions of such nodes to analyze input images. Each node fires or shuts based on the input that it receives and mimics a human mind's neurons working when trying to recognize images. All parallel nodes in the network are further referred to as a layer. DL neural networks are networks with at least two hidden layers. Often, a neural network consists of tens to hundreds of layers (Ren et al. 2016; He et al. 2015). Figure 6 shows a deep neural network with two hidden layers with all input layer nodes fully connected to the next layer.

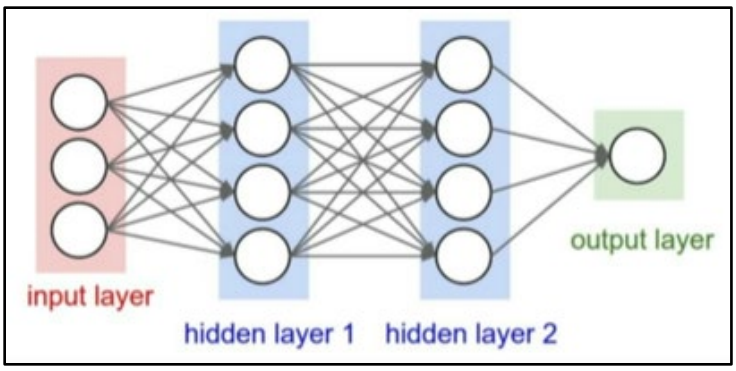

Figure 6. A Convolutional Neural Network. Source: Stanford University Open courseware

The training of CNNs is generally split into supervised and unsupervised training. Supervised training refers to training where the corresponding correct outputs are available for the network to compare and converge to a predictable output. Unsupervised training refers to the training process where the correct output is not available. In this study, all training done are supervised training to guarantee performance of the model.

B. COMPUTER VISION TASKS

The most common tasks related to computer vision is in classification of images to certain categories. For example, automatically classifying wild animals that roam a pre-defined habitat area. CNN is one of the most common algorithms for DL tasks with image classification. It uses convolution filters to extract features from the image to learn and perform classification. Figure 7 shows a simplified view of the CNN's architecture. The image is fed into the network which consists of many convolutional layers which extract different features like edges and colors, from the image to generate a feature map of the images. Using these feature maps and ReLU activation functions, the network is able to allocated certain probabilities of each feature map's relation to the intended classification categories. Finally, depending on the number of classes the network is supposed to predict, the network maps probability scores for each class and the class with the highest score will be the image's class.

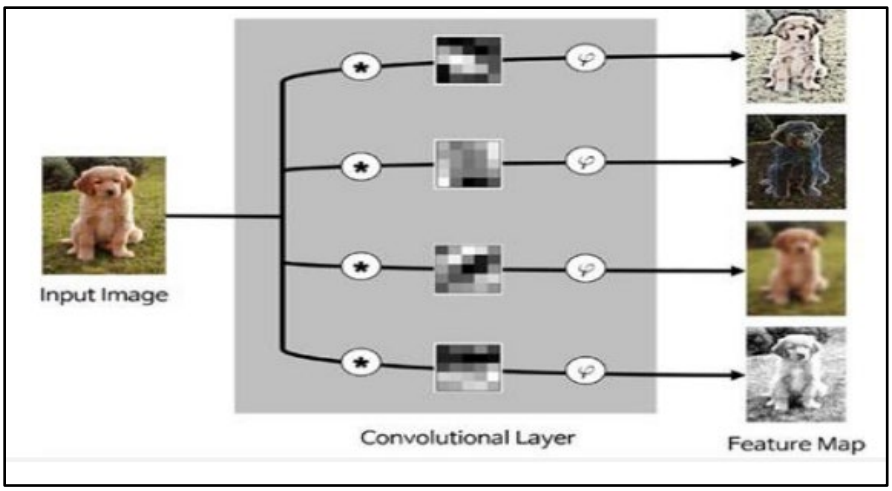

Figure 7. Architecture of Convolutional Neural Network. Source: Kim (2017, 125).

Other than classification, the CNN could also have continuous values as an output. In this aspect, the task fulfilled is a regression task as the input image eventually generates a value at the end of the training. Regression networks are useful when an estimated value is required instead of a class. For example, estimating the income levels of a certain population group by age is a regression task.

On top of classification and regression that is the focus of this study, other examples of computer vision tasks are object detection and instance segmentation. These are frequently employed in self-driving cars and human-machine interactions where it is important to differentiate between a living object and other non-living object. In object detection, images with objects are detected with a certain confidence level of its class and a bounding box. See Figure 8 for an illustration of an objection detection task. It is important to note here that prediction is based on probabilistic estimation and not definitive. Hence, safety margins would be required for a safe implementation in real world scenarios to handle outlying cases.

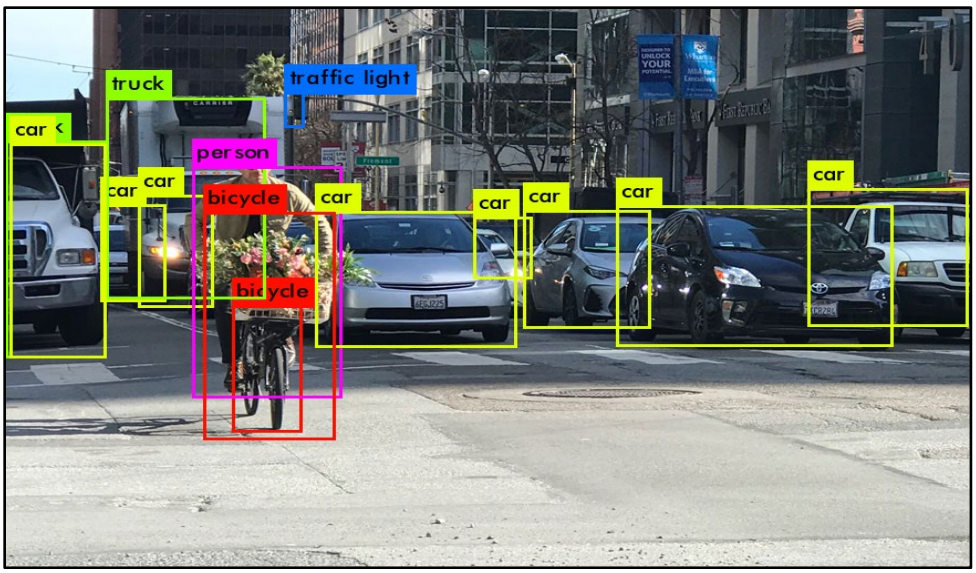

Figure 8. Object Detection in Self-driving Cars. Source: Archie Shou (2020).

C. WAVEFRONT PREDICTION AND CORRECTION

With the computer's ability to "see" images and derive relationships between the input images and expected output, the task of wavefront prediction and correction can be fulfilled using DL. First, the CNN can be fed images with known atmospheric turbulence induced aberrations (modelled with 33 term Zernike polynomials) and a prediction can be derived by the trained CNN. Second, the CNN can be used to deduced blurred images given correct clear pristine images as reference training material.

There are broadly two different types of wavefront sensing approaches. The first is aperture plane (direct) sensing and second is image plane (indirect) sensing (Murray 2006). Direct wavefront sensing requires a device like the Shack-Harmann wavefront sensor previously mentioned to detect the wavefront error using the incoming image as a basis. On the other hand, indirect methods do not directly measure the wavefront. It deduces the wavefront by using relevant information and passes correction parameters to the DM directly. An example is by sharpening the image directly to produce a pristine image for use. Using DL to predict wavefronts is a type of indirect wavefront prediction method.

D. REVIEW OF RESNET

The Residual Network (ResNet) was introduced by (He et al. 2015) for image classification using deeper neural networks. While the ResNet was substantially deeper than other neural networks proposed, it was easier to train and optimize because of its lower complexity. This network was used for image classification in ImageNet test set and won the 1st place on the ImageNet Large Scale Visual Recognition Challenge (ILSVRC) 2015 classification task. Due to its success and accuracy in image classification, this network was chosen for our study and modified for regression tasks.

The main feature of the ResNet is a residual learning block which bypasses certain number of layers such that the original data is still retained. These short-cut connections do not add additional learnable parameters or contribute to the complexity of the computation, which makes the network trainable with lesser time and resources.

E. REVIEW OF U-NET

The U-Net is a CNN used for biomedical image segmentation. It consists of an encoder and decoder subnetwork that are connected by a bridge section which enables strong data augmentation in training the network. This network could be used to train from start to end using very few images and yet still outperforms other networks in image segmentation of electron microscopic stacks (Ronneberger, Fischer, and Brox 2015). This network allows image to image regression tasks, which was used for image correction of a blurred image to a clear pristine image for improving target tracking. Furthermore, the input image layer of the U-Net is customizable, which affords flexibility in different input sizes and hence is more versatile to be deployed on different images sources.

The main features of the U-Net are the ability to obtain good training results even with little image dataset. The simplicity of the network also means that the network is sufficiently fast for close to real time applications in the context of target tracking or HEL beam propagation.

THIS PAGE INTENTIONALLY LEFT BLANK

IV. APPROACH OF STUDY

This chapter describes some of the mathematical methodologies and theories behind this study including some important performance measures for image correction applications in HEL systems. The chapter starts off with description on how atmospheric turbulence is modelled mathematically using 33 term Zernike polynomials by representing phase value using a linear combination of base functions. Thereafter, turbulence strength and performance measures like the Fried parameter, r_o, and Strehl ratio, s, is explained. Finally, the chapter ends with an evaluation of the limitations of the approach of research and real-world application constraints which will require physical testing to validate the effectiveness of the model.

A. MODELLING TURBULENCE USING ZERNIKE POLYNOMIALS

The most common method to represent atmospheric turbulence effects on a beam is through the use of Zernike polynomials. Zernike polynomials are a sequence of polynomials that are orthogonal on the unit disk (Schwiegerling 2017). Expressed conveniently in polar coordinates r and θ, the polynomials are the product of an angular function and radial polynomials. The radial polynomials are derived from the Jacobi polynomials while the angular functions are basis functions for the two-dimensional rotation group. This research used Noll's coefficients (Noll 1976) to represent varying atmospheric turbulence effects using Zernike polynomials. The Zernike polynomials are defined as

$$\left.\begin{aligned} Z_{even,j} &= \sqrt{n+1}R_n^m(r)\sqrt{2}\cos m\theta \\ Z_{odd,j} &= \sqrt{n+1}R_n^m(r)\sqrt{2}\sin m\theta \end{aligned}\right\} m \neq 0$$
$$Z_j = \sqrt{n+1}R_n^0(r), m = 0 \qquad . \qquad (4)$$
$$where, R_n^m(r) = \sum_{s=0}^{(n-m)/2} \frac{(-1)^s (n-s)!}{s!\left[(n+m)/2-s\right]!\left[(n-m)/2-s\right]!} r^{n-2s}$$

The values of m and n satisfy $m \le n$, $n - |m| = even$. The index j is a mode ordering number and is a function of n and m.

With the Zernike polynomial coefficients, the corresponding wavefront can be constructed. The wavefront is an "imaginary surface representing corresponding points of a wave that vibrate in unison" (Encyclopedia Britannica n.d.). Figure 9 shows the Zernike polynomials and the respective shape of wavefront.

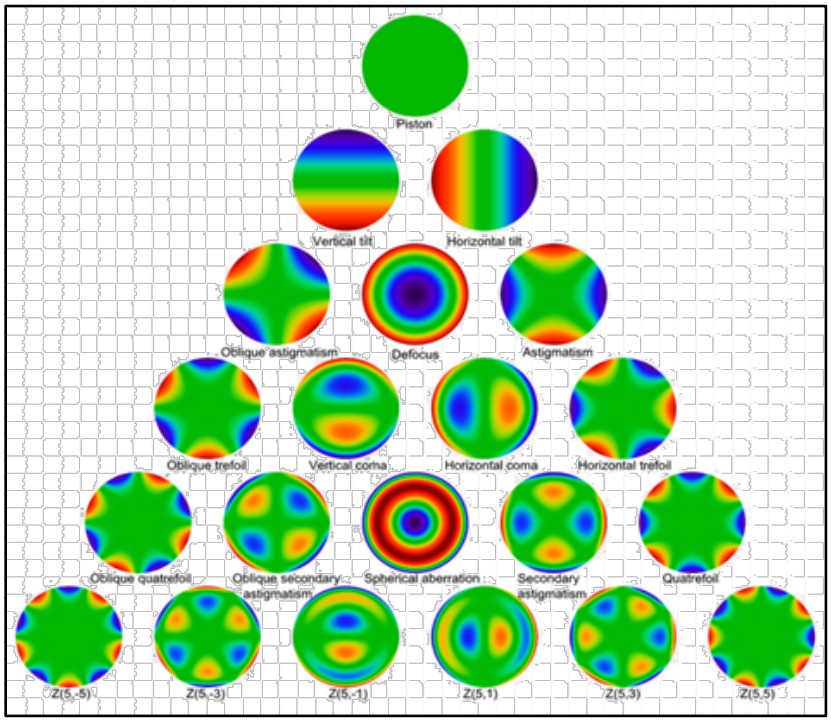

Figure 9. Zernike Polynomials. Source: Sirena (n.d. *https://cleanpng.com*).

This study uses 33 term Zernike polynomials to model atmospheric turbulence. The first three terms - piston, vertical tilt, horizontal tilt - are eventually omitted in the results since these three terms are usually associated with target tracking and if the target is not tracked, the model should not generate any predictions.

B. DATA GENERATION

Using randomized coefficients of Zernike polynomials over a normal distribution with mean and variance determined experimentally (Noll 1976), a 33 term Zernike polynomial representation of atmospheric turbulence is generated. With this Zernike polynomial representation of atmospheric turbulence, the corresponding wavefront is constructed, and the Point Spread Function (PSF), h, obtained. The wavefront, w, is represented with the 33 term Zernike polynomial, z_i, with the normally distributed coefficients a_i.

$$w(r,\theta) = \sum_{i=1}^{\infty} a_i z_i(r,\theta) \tag{5}$$

Here, r is the radial distance and θ is the azimuthal angle in polar coordinates. The PSF, h is transformed using the Fourier transform, F

$$h = \left| F[w] \right|^2 \tag{6}$$

Finally, the target scene of interest, f, is convolved with the PSF, h, giving the blurred image g.

$$g = h \otimes f \tag{7}$$

These generated data of Zernike polynomials, wavefronts and the corresponding PSF and are used in this research extensively. Hence it is necessary to first explain the process of data generation and its usage. First, the PSF is simulated using a distant point light source at diffraction limit. The PSF (input image) and the 30 term Zernike polynomial (output) are used to predict the correct Zernike polynomials coefficients using the modified ResNet-18 CNN architecture. Second, the PSF images from the first part is convolved with the UAV images dataset available at NPS to generate blurred extended point source images with **known** Zernike polynomials coefficients from the first part. This is important since the availability of known Zernike polynomials coefficients in real-world scenarios are rare which makes simulations like this resource efficient and effective. Thirdly, the blurred UAV images are used as inputs to the Unet CNN and the original clear UAV images as

outputs for direct image to image correction without using Zernike polynomials. Table 2 shows the training parameters that were used to generate the images used for training.

Table 2. Summary of Training Parameters Used

Parameter	Values	Additional Information (If Any)
Aperture Size / m	0.3	Size of Telescope
Grid Size	224x224x3	- Black and white images: Repeated in three channels - RGB images: Stacked images with different defocus levels 0,5 and 10
Wavelength, λ / μm	1.0	Laser beam wavelength
Target Distance, z / m	4,000	-
r_o / m	0.01 to 0.1	-
Number of Images	20,000	-

1. Point Source Images

As an initial simulation baseline, 20,000 PSF images were created using 33-term Zernike polynomials for training as described above. The first three terms (piston, vertical tilt, and horizontal tilt) from the results were set to zero since the target would need to be within the optical device's line of sight for initial application. A sample of the 30 term Zernike and the corresponding PSF image is shown in Figure 10.

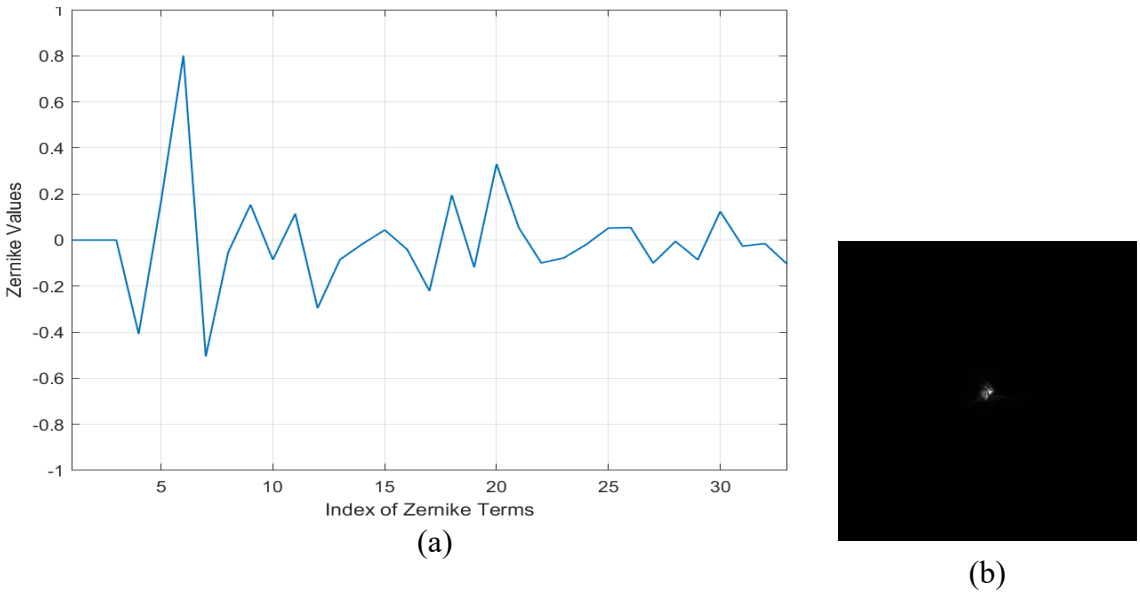

(a) (b)

Figure 10. Example of PSF Images Generated for Simulation: Zernike Polynomials (a), and Corresponding PSF image (b)

2. UAV Images

The second set of images generated were blurred UAV images. A dataset of 200,000 clear pristine simulated Reaper and Mongoose UAV target images were available at NPS for use. These UAV images were convolved with the PSF images created in the first part to generate a corresponding blur UAV image with known Zernike polynomials. This dataset was then used for the second and third part of the study for UAV images Zernike prediction and direct image correction. The respective Zernike polynomials were also tagged to the blurred images for results comparison. Figure 11 shows a sample of the UAV images generated.

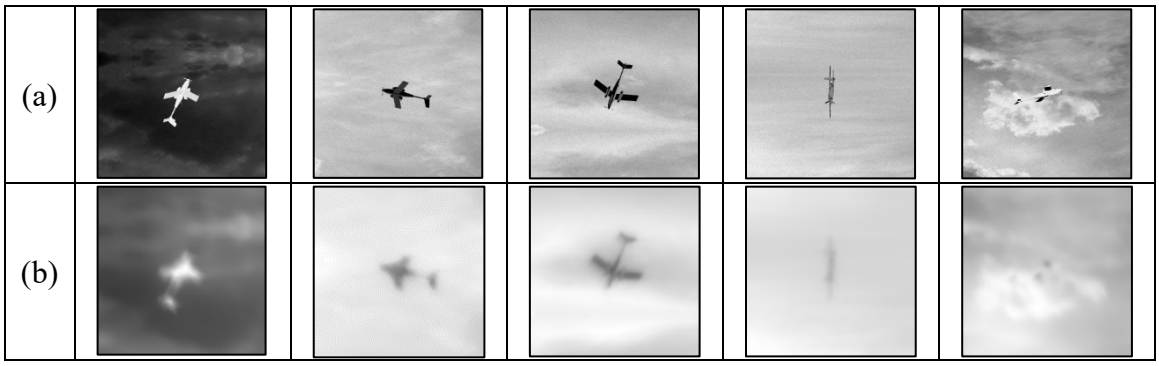

Figure 11. Example of UAV Images Generated for Simulation: Original clear UAV Images (a), Blurred UAV Images with Zernike Polynomial Recorded (b)

C. NUMERICAL MEASURES

1. Fried Parameter, r_0, and Strength of Turbulence, C_n^2

The Fried parameter, r_0, is a measure of the quality of light transmission through the atmosphere due to turbulence effects. Typical Fried parameter that gives good image quality is about 20 to 40cm (Axtell 2014). The value of 10cm was selected for initial investigation and smaller value (more turbulence) ranges were used to test the effective limit of the DL model in predicting and correcting images with r_0 up to 1cm. The corresponding refractive structure constant, C_n^2, is related to the Fried parameter (Fussman 2014) by the equation

$$r_0 \approx 0.33 \frac{\lambda^{6/5}}{\left(d^{3/5} C_n^2\right)^{3/5}}, \tag{7}$$

where λ is the wavelength of the laser, d is the target distance. Typical values for the strength of turbulence, C_n^2, is $10^{-17}\text{m}^{-2/3}$ and $10^{-13}\text{m}^{-2/3}$ for weak and strong turbulence, respectively (Fussman 2014). In this work, varying r_0 and C_n^2 conditions are simulated with the Zernike polynomial coefficients representation of atmospheric turbulence.

2. Strehl Ratio

The Strehl ratio is a "measure of the quality of optical image formation" originally proposed by Karl Strehl (Strehl 1902). It is used in imaging through atmospheric turbulence as a measure of the aberration and has a range between zero to one. With one representing a hypothetically perfect clear image. The ratio is used to compare against an ideal case where the laser beam is un-aberrated and estimate the effectiveness of the laser beam at the target. A simplified Strehl ratio can be calculated (Sacek 2006) as

$$S \approx \frac{1}{e^{(2\pi\omega)^2}}, \tag{8}$$

where e is the natural logarithm base and ω is the Root Mean Square wavefront error. The Strehl ratio is also used in the work to represent the wavefront estimation error from deep learning algorithms.

THIS PAGE INTENTIONALLY LEFT BLANK

V. SIMULATION RESULTS AND POTENTIAL ERRORS

In this chapter, the simulation results using different input images to obtain the wavefronts are presented. The first type of images used is PSF images generated using Zernike polynomials. The second type of images is UAV images that are convolved with the PSF images to generate a dataset with blur UAV images and their respective Zernike polynomials. Finally, the CNN is trained directly using image to image regression to obtain a clear image. All training used 20,000 images from the overall set of 200,000 images.

A. POINT SOURCE IMAGES

The PSF images generated were used to train the ResNet-18 CNN to output the expected 30 term Zernike polynomial. The prediction accuracy was found to be poor. Other than using a focused PSF image, defocus was also added to the PSF image to simulate phase diverse data for simulation. Figure 12 shows the PSF image from Figure 9 with an added defocus level of 5, 10 and 20 in the focus term of Zernike polynomials. Due to the nature of image recognition-related DL and the computer "seeing" these images, the prediction results obtained was best when defocus was added. This likely gave the network more information to predict and estimate the Zernike polynomials compared to the focused PSF image which has little information all concentrated in a few pixels in the middle of the image.

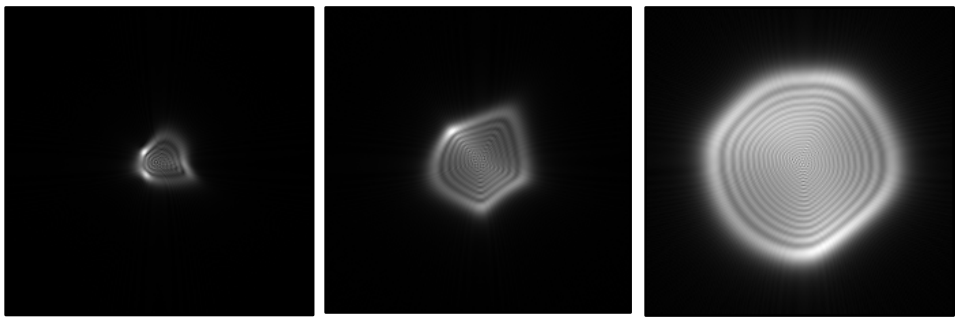

(a) (b) (c)

Figure 12. PSF Image with Defocus Added of 5 (a), 10 (b), and 20 (c)

Simulations for three defocus levels at 5, 10, 20 were run. Other than adding defocus to increase the amount of pixel information in the image, three layers of zero, five, and 10 defocus levels were stacked together to form the three channels of the RGB image for a final run to test the estimation accuracy for images containing different phases. Table 3 summarizes the training results. Clearly the increase in the level of defocus added helped improve the training and validation errors. Nevertheless, the contribution to accuracy by adding of defocus reaches a diminishing value once the majority of the pixels in the image are filled up.

Table 3. PSF Image Training Results for $\mathbf{r_0}$**=10cm** and Added Defocus

Level of Defocus	Training RMSE	Validation RMSE	RMS Wavefront Error / e-04	Corresponding Strehl Ratio
No Defocus	1.2576	1.2606	22	0.973
+ 5	0.4262	0.4167	6.79	0.992
+ 10	0.2732	0.2724	4.54	0.994
+ 20	0.2276	0.2115	3.46	0.996
Stacked image with three levels of defocus 0,5,10	0.3176	0.3137	5.08	0.994

A closer look at the training results indicates that without defocus added, the model is unable to predict well the Zernike polynomials and the results were unable to be used in HEL systems for wavefront correction. Figure 13 shows the overall scatter plot for the complete dataset of 20,000 training PSF images.

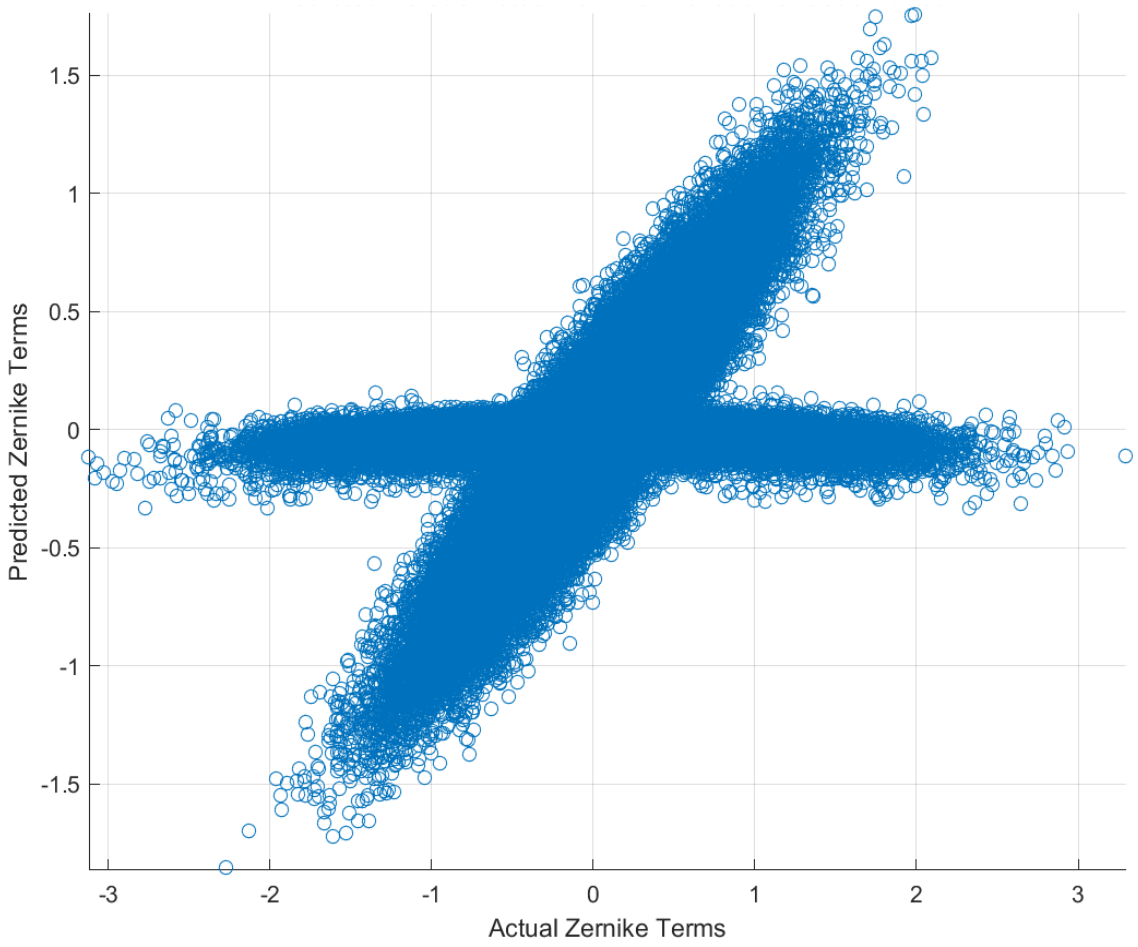

Figure 13. Scatter Plot of PSF Images Predicted versus Actual Zernike Polynomials—No Defocus Added

From Figure 13, it is observed that the predictions for a focused PSF image causes false predictions along the entire spectrum of 30 Zernike Coefficients. Due to the likely lack of information in a focused PSF image, 8.6% of the predicted Zernike terms were near zero and failed in predicting a reasonable Zernike value. In contrast, the added defocus of 20 helped improved the estimation results and gave a much better prediction of the Zernike Coefficients to generate the wavefronts. Figure 14 shows this improvement where the prediction error standard deviation was 0.0337 compared to 0.163 in the case where no defocus was added.

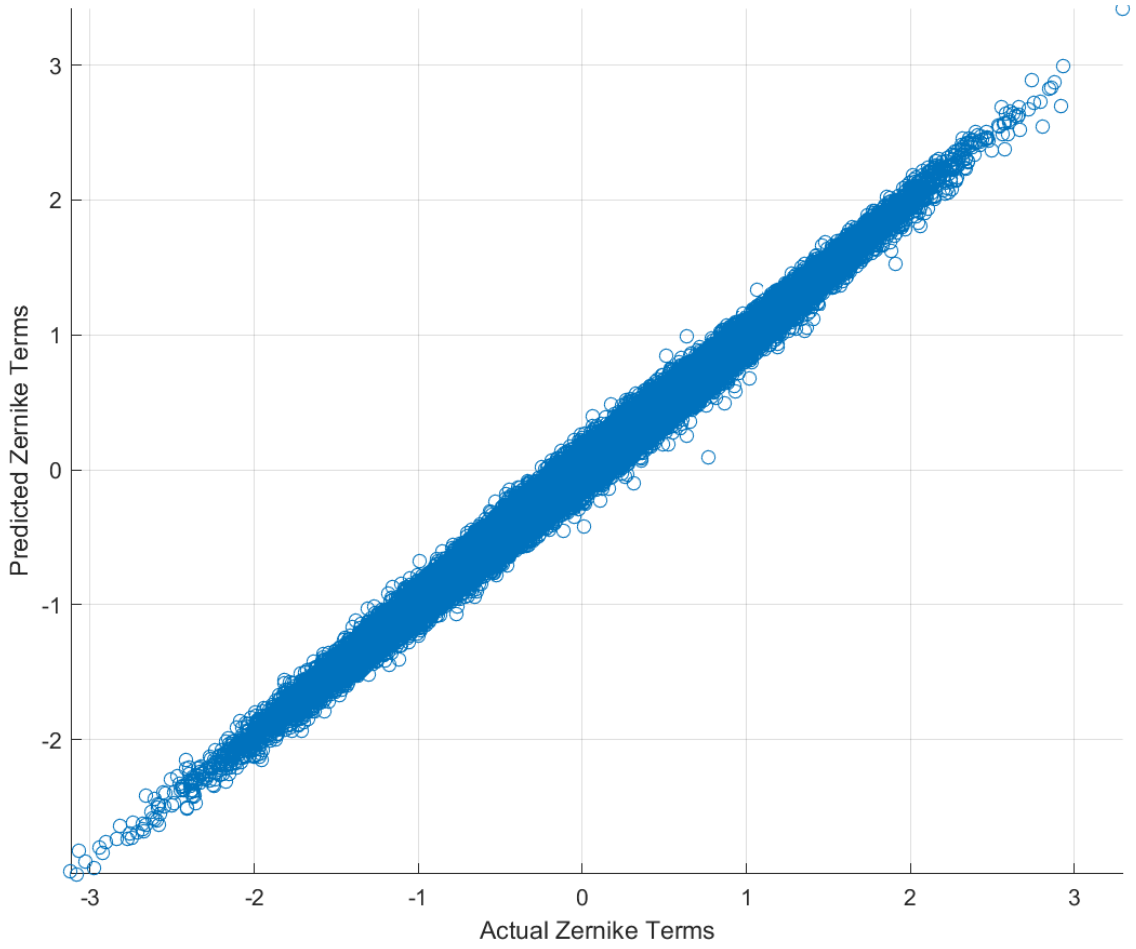

Figure 14. Scatter Plot of Predicted versus Actual Zernike Coefficients with +20 Defocus

Using the best results for added defocus of 20, the CNN model was used to test against a new generated test set of up to 1,000 PSF images. A sample of the prediction results is shown in Figure 15. Prediction is highly accurate and predicting time was about 54ms[1] per image, slightly more than 33ms for real-time processing.

[1] Using a standard laptop computer with i3 CPU, 8GB of RAM and integrated graphics card.

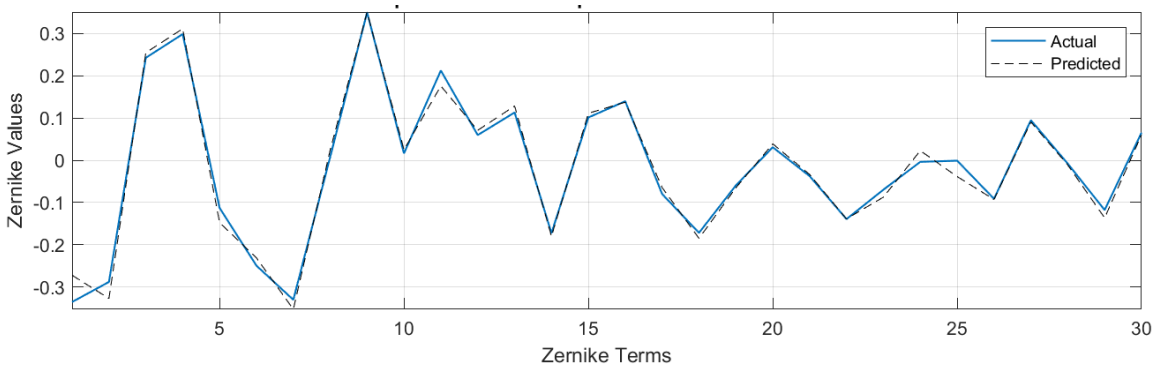

Figure 15. Sample of Predicted Zernike Coefficients for PSF Images with Added Defocus +20

Given the close approximation of the actual Zernike Coefficients in the predicted values, the predicted wavefront also closely resembles the actual wavefront as illustrated in Figure 16.

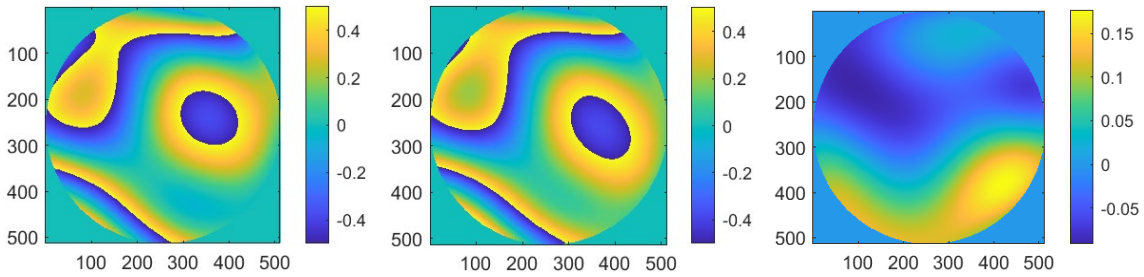

(a) (b) (c)

Figure 16. Generated PSF Images of Actual Wavefront (a), Predicted Wavefront (b), and Wavefront Error (c)

Building on the good results from r_0=10cm, further simulation was run to test the limits of the model in strong turbulence by setting the r_0 values from one to five, with one being the strongest turbulence. The results start to fail at r_0 smaller than 2cm as the Strehl ratio drops significantly over the range of r_0 values. Table 4 provides a summary of the results of varying r_0 values.

Table 4. PSF Image Training Results for **r_0=1 to 5cm** Stacked Images

r_0 /cm	Training RMSE	Validation RMSE	RMS Wavefront Error / e-3	Corresponding Strehl Ratio
1	28.564	48.551	82.7	0.354
2	5.807	8.072	13.3	0.846
3	2.603	3.024	4.6	0.944
4	1.562	1.676	2.5	0.969
5	1.090	1.032	1.6	0.980

B. EXTENDED POINT SOURCE UAV IMAGES

While PSF images are useful as a first approximation and proof-test of the simulation method, actual UAV images are more practical for use in HEL systems. Hence, the next dataset used is the simulated real-life UAV images from the Reaper and Mongoose UAV target images dataset. These images were convolved with the PSF images previously generated using randomized Zernike polynomials from the first part. A similar approach to the PSF images was adopted to train the ResNet-18 CNN to output the expected 30 term Zernike polynomial. The same parameters were also used as per listed in Table 2.

The same levels of defocus were also added to the UAV images to test the response compared to PSF images. Figure 17 shows the original in-focus UAV images and the respective post-processed images that had defocus added. Images (c) through (f) has no visible differences since the only distinction between them is the level of defocus that was added to the image.

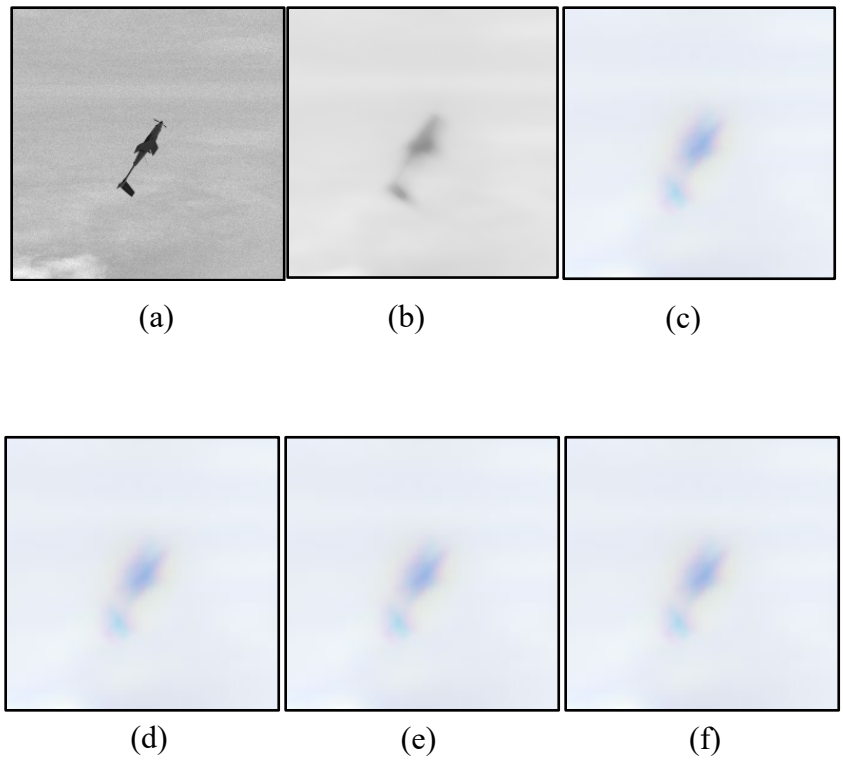

Figure 17. Types of UAV Images Used: Original Clear (a), Blurred No Defocus (b), Defocus +5 (c), Defocus +10 (d), Defocus +20 (e), and Stacked (f)

Defocus was added to increase the amount of information fed into the CNN to improve the accuracy. A total of three other runs were conducted for defocus levels at 5, 10, 20. Finally, three layers of 0, 5, and 10 defocus levels were stacked together to form the three channels of the RGB image for a final run to test the estimation accuracy for images containing different phases. Table 5 summarizes the training results. Clearly the increase in the level of defocus added helped improve the training and validation errors. Nevertheless, the level of defocus added reaches a diminishing value once the majority of the pixels in the image are filled up as in the case with PSF images.

Table 5. Summary of UAV Image Training Results for Added Defocus

Level of Defocus	Training RMSE	Validation RMSE	RMS Wavefront Error / e-3	Corresponding Strehl Ratio
No Defocus	1.5007	1.4807	2.5	0.969
+ 5	1.1007	1.1113	2	0.975
+ 10	1.074	1.0966	1.9	0.976
+ 20	1.224	1.290	2.2	1.000
Stacked image with 3 levels of defocus 0,5,10	0.9774	0.991	1.8	1.000

A closer look at the training results indicates that unlike the outcome for PSF images, the UAV images dataset did not result in better prediction with added defocus. This fits well with the explanation previously since the UAV images already had sufficiently large amount of pixel information in each image unlike the few concentrated pixels in the PSF images with no defocus added. Consequently, the results for using UAV images as inputs was best with stacked images with three different defocus levels compared to the highest defocus level for PSF images. Using UAV images as input likely need a different approach for pre-processing the image to obtain better results. This will be discussed at the end of this chapter on possible improvements.

Similar to PSF images, the predictions for UAV images with no added defocus results in false predictions along the entire spectrum of 30 Zernike Coefficients. This is illustrated in Figure 18. The added defocus helped improved the estimation results and gave a much better prediction of the Zernike polynomials to generate the wavefronts. Figure 19 shows this improvement and all predicted Zernike terms were within standard deviation of 0.165 of the original Zernike coefficients. However, the standard deviation is large and needs to be further improved.

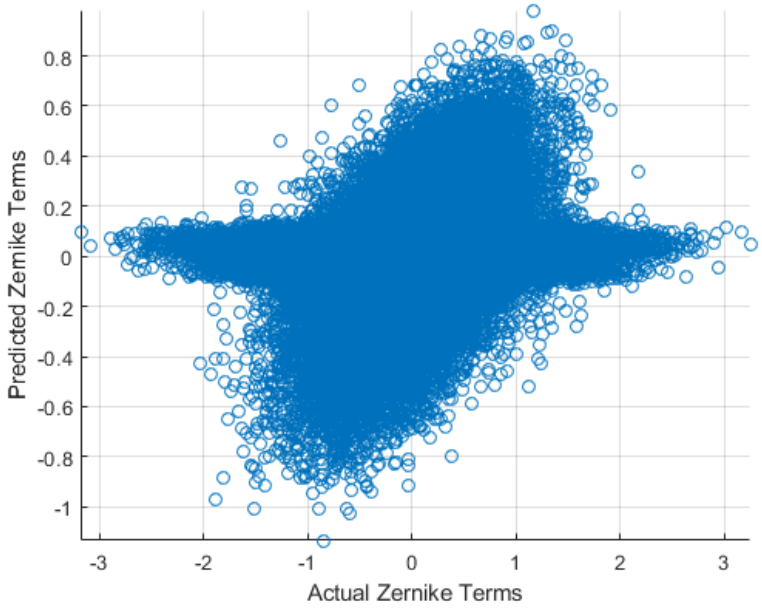

Figure 18. Scatter Plot of UAV Images Predicted Versus Actual Zernike Coefficients—No Defocus Added

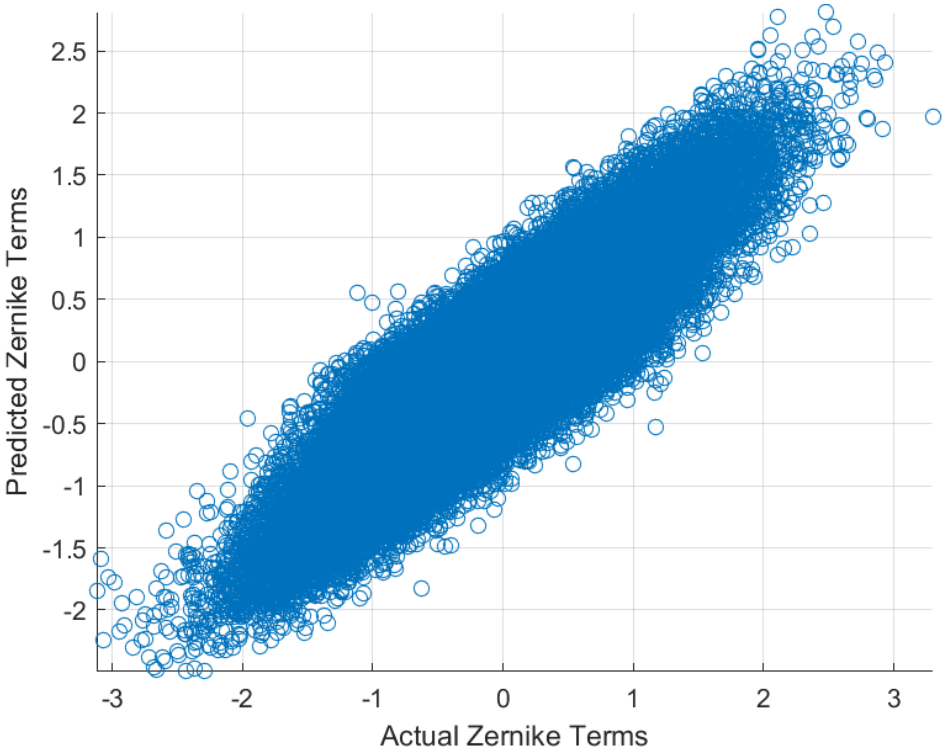

Figure 19. Scatter Plot of Predicted Versus Actual Zernike Coefficients with +20 Defocus

Using the best estimation results in Table 5, for stacked images, the model was used to test against a new generated test set of up to 1,000 PSF images. A sample of the prediction results is shown in Figure 20.

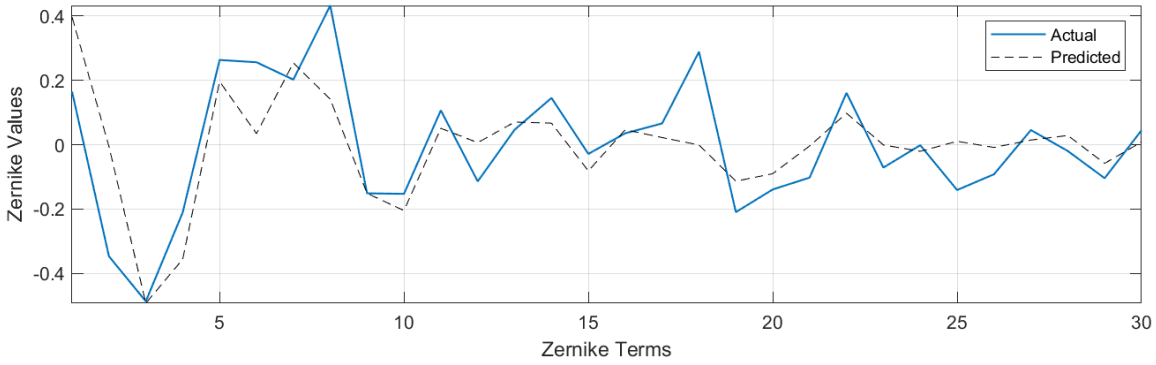

Figure 20. Predicted Zernike Coefficients for Stacked UAV Images

The corresponding predicted wavefronts are illustrated in Figure 21.

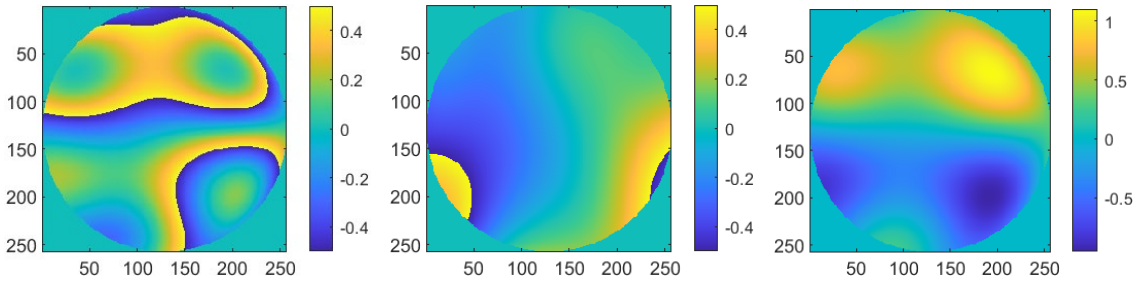

(a) (b) (c)

Figure 21. Results from UAV Images: Actual Wavefront (a), Predicted Wavefront (b), and Wavefront Error (c)

C. DIRECT IMAGE CORRECTION

Other than using Zernike polynomials to model turbulence, the CNN also has the ability to be trained directly for image correction without using Zernike polynomials. This section makes use of the UAV image dataset that was created in the previous part to train

the Unet CNN to take as inputs blurred UAV images and output clear pristine images. A set of 20,000 blurred and clear original images were used for training. Figure 22 shows a sample of these images with the de-blurred image. The Unet CNN was trained to output de-blurred images with clear outputs. The average processing time needed for one image is about 0.9s, which is still some way off the real-time requirements of operational requirements in a naval combat environment. While there is some promise in the CNN's ability to correct blur images and output clear images, the model needs to be further improved to ensure operationality on a naval ship.

(a) (b) (c)

Figure 22. Sample Training UAV Images: Original Clear, Blurred, r_0=10cm (b), and De-Blurred (c)

D. POSSIBLE IMPROVEMENTS

One possible improvement to increase the accuracy of prediction is to include some form of pre-processing integral to the CNN architecture. This would help to filter out unwanted "noise" from the image. Real-world UAV images come with unwanted information like clouds and shadows which increase the complexity of the image and reduce the accuracy of prediction. Pre-processing the image would focus the information processing to the key features of the UAV and would likely result in better prediction accuracy.

The study was confined to dataset of two UAVs—the Mongoose and Reaper UAVs. While the trained networks are still usable for other UAVs, it may not give good results. Training data needs to be general enough to prevent overfitting. Hence, more training data

UAV types may be required to improve the overall applicability of this model for other UAV types.

The used of direct image correction yields good results to give clearer UAV images and the spectrum of application is large. However, the applicability of this method is confined by the long processing time needed. Perhaps a customized CNN specific for this task would reduce the number of parameters in the CNN and reduce the processing time to a more palatable speed for deployment in naval ships.

VI. CONCLUSION AND RECOMMENDATIONS

The results from this study indicate that AI could be utilized as a means to correct images for atmospheric turbulence so that the corrections can be applied to laser beams to improve the HEL system's effectiveness against intended targets. First, PSF images were used for testing the feasibility of the CNN model and this was further applied to simulated real-life UAV images with limited success. Further improvements need to be integrated to enhance the effectiveness for UAV images. Finally, it was shown that CNNs could be used to directly correct a blurred image to give a clear image. However, real-time image correction is not completely achievable given the need to process large amounts of image information before correction can be done.

A. PSF IMAGES

The results from the first part of the study indicates that the CNN networks work best when more information is presented to the network. The initial poor results from the PSF images with no defocus added had very little information all concentrated in the middle of the image and the rest of the image has no useful information for the network. Thus, prediction results were inaccurate and could not be used to obtain a reasonable model for use. With the adding of defocus, the image size is "enlarged," and additional aberration features added to the image. This helped improve the accuracy drastically and prediction was very accurate for moderate to strong levels of turbulence. This hypothesis was further enforced when the levels of defocus added helped further improve the prediction accuracy. The highest defocus level added gives best results.

B. UAV IMAGES

While the prediction results for PSF images improved with defocus levels, this outcome was not replicated in the UAV images training dataset. The likely cause of this is the complexity of an UAV image compared to a PSF image. Viewed in totality, the PSF image resembles closely a binary output of 1s and 0s depending on the shade of the pixel. However, the UAV image consists of higher order data types like clouds in the atmosphere, UAV silhouette, features of the UAV structure which was not easily distinguishable from

the target of interest. Thus, the prediction results for UAV images were poorer than PSF images. This is also largely in-line with intuition.

C. DIRECT IMAGE TO IMAGE PREDICTION

In image-to-image direct prediction of clear images, the results were accurate. Although at stronger turbulence of $r_0 < 4$cm, the model does not work well as the UAV image is almost indistinguishable from the original image. Without traces of the original UAV image as a guide, the network is unable to miraculously predict the existence of a target.

D. RECOMMENDATIONS AND FUTURE WORK

Finally, the applicability of AI in HEL correction and target tracking had been proven in the simulation environment and some realistic UAV datasets. To further improve the accuracy of the model and real-world scenarios, laboratory tests using actual laser systems are useful for evaluating the effectiveness of the CNN model before full implementation in the field for real-world testing. Further work is also required to customize CNNs for use in real-world images before its implementation in actual HEL systems. Some possible improvements are to integrate some level of pre-processing such that the features of the UAV image are first enhanced through some masking function before feeding it into the CNN for prediction. This may potentially improve target tracking and prediction accuracy. This also makes the UAV image output closer to a PSF image's binary information layer which makes prediction easier with lesser noise in the image.

LIST OF REFERENCES

Ang, Ching Na. 2012. "Analysis of High Energy Laser Weapon Employment from a Navy Ship." Master's thesis, Naval Postgraduate School. http://hdl.handle.net/10945/17314.

Axtell, Travis W. 2014. "Wavefront Reconstruction and Mirror Surface Optimization for Adaptive Optics." Master's thesis, Naval Postgraduate School. http://hdl.handle.net/10945/42576.

Bahman, Zohuri. 2016. *Directed Energy Weapons: Physics of High Energy Lasers (HEL)*. New York: Springer Science+Business Media.

Corley, Melissa S. 2010. "Maritime Adaptive Optics Beam Control." Master's thesis. Naval Postgraduate School. http://hdl.handle.net/10945/10559.

Fussman, Chris R. 2014. "High Energy Laser Propagation in Various Atmospheric Conditions Utilizing a New, Accelerated Scaling Code," June, 114. http://hdl.handle.net/10945/42628.

He, Kaiming, Xiangyu Zhang, Shaoqing Ren, and Jian Sun. 2015. "Deep Residual Learning for Image Recognition." *ArXiv:1512.03385 [cs.CV]*. http://arxiv.org/abs/1512.03385.

IBM Cloud Education. 2021. "What Is Artificial Intelligence (AI)?" IBM Cloud Education. April 7, 2021. https://www.ibm.com/cloud/learn/what-is-artificial-intelligence.

Kim, Phil. 2017. MATLAB Deep Learning: With Machine Learning, Neural Networks and Artificial Intelligence. For Professionals by Professionals. Berkeley, California: Apress.

Liu, Minzhao, David N. Lopez, and Gabriel C. Spalding. 2020. "Experimental Implementation of Wavefront Sensorless Real-Time Adaptive Optics Aberration Correction Control Loop with a Neural Network." SPIE 11469, Emerging Topics in Artificial Intelligence 2020, 114691S (20 August 2020). https://doi.org/10.1117/12.2569647.

Murray, Larry P. 2006. "Smart Optics: Wavefront Sensor-Less Adaptive Optics - Image Correction through Sharpness Maximisation." PhD dissertation. National University of Ireland. https://www.osapublishing.org/abstract.cfm?uri=FiO-2006-FMF3.

Nishizaki, Yohei, Matias Valdivia, Ryoichi Horisaki, Katsuhisa Kitaguchi, Mamoru Saito, Jun Tanida, and Esteban Vera. 2019. "Deep Learning Wavefront Sensing." *Optics Express* 27 (1): 240. https://doi.org/10.1364/OE.27.000240.

Noll, Robert J. 1976. "Zernike Polynomials and Atmospheric Turbulence*." *Journal of the Optical Society of America* 66 (3): 207. https://doi.org/10.1364/JOSA.66.000207.

O'Rourke, Ronald. 2015. "Navy Shipboard Lasers for Surface, Air, and Missile Defense," CRS Report No. RL41526. Washington, DC: Congressional Research Service. https://fas.org/sgp/crs/weapons/R41526.pdf.

Palmer, A. Jay. 1980. "Nonlinear Optics in Aerosols." *Optics Letters* 5 (2): 54. https://doi.org/10.1364/OL.5.000054.

Puent, Donald. 2017. "Integration of Adaptive Optics into High Energy Laser Modeling and Simulation," Master's thesis. Naval Postgraduate School. http://hdl.handle.net/10945/55520.

Ren, Shaoqing, Kaiming He, Ross Girshick, and Jian Sun. 2016. "Faster R-CNN: Towards Real-Time Object Detection with Region Proposal Networks." *arXiv:1506.01497 [cs.CV].* http://arxiv.org/abs/1506.01497.

Ronneberger, Olaf, Philipp Fischer, and Thomas Brox. 2015. "U-Net: Convolutional Networks for Biomedical Image Segmentation." *arXiv:1505.04597 [cs.CV]*. http://arxiv.org/abs/1505.04597.

Sacek, Vladimir. 2006. "Notes on Amateur Telescope Optics." July 14, 2006. https://www.telescope-optics.net/Strehl.htm.

Schwiegerling, Jim. 2017. "Review of Zernike Polynomials and Their Use in Describing the Impact of Misalignment in Optical Systems." In *Optical System Alignment, Tolerancing, and Verification XI*, edited by José Sasián and Richard N. Youngworth, 13. San Diego, United States: SPIE. https://doi.org/10.1117/12.2275378.

Strehl, Karl. 1902. "Ueber Luftschlieren Und Zonenfehler." *Zeitschrift Für Instrumentenkunde* 22 (July): 213–17.

Valiani, Joshua H. 2016. “Power and Energy Storage Requirements for Ship Integration of Solid-State Lasers on Naval Platforms,” June, 62.

Xu, Yangjie, Dong He, Qiang Wang, Hongyang Guo, Qing Li, Zongliang Xie, and Yongmei Huang. 2019. “An Improved Method of Measuring Wavefront Aberration Based on Image with Machine Learning in Free Space Optical Communication.” *Sensors* 19 (17): 3665. https://doi.org/10.3390/s19173665.

THIS PAGE INTENTIONALLY LEFT BLANK

INITIAL DISTRIBUTION LIST

1. Defense Technical Information Center
   Ft. Belvoir, Virginia

2. Dudley Knox Library
   Naval Postgraduate School
   Monterey, California